Batteries & Supercaps

Research Article
doi.org/10.1002/batt.202300331

Chemistry Europe
European Chemical Societies Publishing

www.batteries-supercaps.org

Design of L-asparaginasespacer Molecules Intercalated 2D Ti_2C with Increased Interlayer Spacing towards High-performance Sodium-ions Storage

Dong-Ting Zhang[+],[a, b] Bei Zhao[+],[a, b] Hao Chen,[a, b] Zi-Zhou Yuan,*[a, b] Cheng-Gong Chang,*[c, d] and Mao-Cheng Liu*[a, b]

MXenes are promising insertion-type two-dimensional (2D) anode materials for rechargeable sodium-ions batteries owing to unique layered structure, tunable interlayer spacing, and abundant surface functional groups. However, MXenes suffer from inevitably self-stacking and narrow interlayer spacing, leading to the limited utilization of layered structure and sluggish ions diffusion kinetics. Herein, the (L-asparaginase) LAG molecules as intercalation spacers were intercalated into the interlayer of Ti_2C by hydrogen-bond interaction and electrostatic interaction to prepare the intercalated Ti_2C by LAG molecules (named as LAG-Ti_2C). The LAG-Ti_2C not only avoids self-stacking and broadens interlayer spacing to maximumly utilize the layered structure, but also buffers the volume expansion via the pillar effect of intercalated LAG molecules. Such LAG-Ti_2C could remarkably enhance the cycling stability and rate capability of Na^+ ions storage. A decent specific capacity of 113.5 mAh g^{-1} and high capacity retention of ~98.7% at 0.1 A g^{-1} after 1000 cycles can be presented. In addition, the LAG-Ti_2C//AC sodium-ions capacitor (SIC) delivers a high energy density of 27.56 Wh kg^{-1} at power density of 3937.1 W kg^{-1}. The work promotes the further development of layered MXenes and optimizes electrochemical performance of sodium-ions storage via the strategy of intercalating spacers.

Introduction

MXenes have attracted ever-increasing attention in electrochemical capacitors and batteries owing to unique layered microstructure, excellent metal conductivity, outstanding mechanical stability, abundant surface functional groups, and tunable interlayer spacing.[1–4] However, as with other two-dimensional (2D) materials, MXenes deliver inevitably self-stacking between the adjacent nanosheets layers and narrow interlayer spacing due to exceptional strong van der Waals forces, which resulted in the limited active sites for ions storage and sluggish ions diffusion kinetics.[5–10] These bottleneck factors constrain the accessibility of alkali metal ions and prevent rapid ions diffusion between 2D interfaces, ultimately impairing the cycle stability and rate capability of MXenes.[11,12] Hence, restraining self-stacking and widening interlayer spacing is crucial to optimize electrochemical performance of MXenes and excavate utilization potentiality of layered structure.

The strategy of intercalation spacers between the MXenes nanosheets have stood out as an excellent approach for boosting the utilization of layered structure. Cation (such as Sn^{2+}, Zn^{2+}, Mg^{2+}, NH^+)[13–16] and organic molecules (including acetonitrile, CTAB, dimethyl sulfoxide, N,N-dimethylacetamide)[17,18] can spontaneously intercalate MXenes as spacers to effectively restrain restacking and increase interlayer spacing, improving the electrochemical performance of alkali metal ions storage. The pillared Co,[19] Al,[20] and Si[21] atoms between the interlayer of MXenes not only contribute the effects of spacers, but also relieve the consumption of electrolyte via forming stable and thin SEI film on electrode surface. The 0D/1D/2D nanomaterials as spacers can also effectively reduce van der Waals forces to further optimize the utilization of MXenes layered structure, such as Co_3O_4 nanoparticles,[22,23] MoS_2 nanosheets,[24,25] graphene,[26] carbon nanotubes,[27,28] and $FePS_2$ nanosheets,[29] and 1D CoTe.[30] In addition, a variety of fatty diacid and aromatic diacid molecules with different molecular lengths have been employed as pillars to address these inherent disadvantages of MXenes through molecular welding process.[31–33] The above methods have been proved which can effectively prevent self-stacking and enlarge the

[a] D.-T. Zhang,[+] B. Zhao,[+] H. Chen, Prof. Z.-Z. Yuan, Prof. M.-C. Liu
State Key Laboratory of Advanced Processing and Recycling of Non-ferrous Metals
Lanzhou University of Technology
Lanzhou 730050 (P. R. China)
E-mail: yuanzz@lut.edu.cn
liumc@lut.edu.cn

[b] D.-T. Zhang,[+] B. Zhao,[+] H. Chen, Prof. Z.-Z. Yuan, Prof. M.-C. Liu
School of Materials Science and Engineering
Lanzhou University of Technology
Lanzhou 730050 (P. R. China)

[c] C.-G. Chang
Key Laboratory of Comprehensive and Highly Efficient Utilization of Salt Lake Resources
Qinghai Institute of Salt Lake
Chinese Academy of Sciences
Xining 810008 (China)
E-mail: ccg168@126.com

[d] C.-G. Chang
Key Laboratory of Salt Lake Resources Chemistry of Qinghai Province
Xining 810008 (China)

[+] These authors contribute equally to this work.

Supporting information for this article is available on the WWW under https://doi.org/10.1002/batt.202300331

Research Article
doi.org/10.1002/batt.202300331
Chemistry Europe
European Chemical Societies Publishing

utilization of layered structure, resulting in improving the cycling stability and rate capability of MXenes. However, it is still a challenge to maximumly utilize the layered structure of MXenes via simultaneously avoiding self-stacking, increasing interlayer spacing, and stabilizing layered structure.

In this work, the Ti_2C intercalated by (L-asparaginase) LAG molecules were constructed via hydrogen-bond and electrostatic interaction to avoid self-stacking, expand interlayer spacing, and relieve volume expansion. The LAG molecules were intercalated into the interlayers of Ti_2C, contributing pillar effect to 2D layered structure. The pillar effect can not only efficiently reduce van der Waals forces between the Ti_2C interlayers to avoid self-stacking and increase interlayer spacing, but also improve the stability of layered structure via relieving structural expansion during Na^+ ions insertion process. In this design, the LGA-Ti_2C used as the anode materials realize outstanding cycle stability and superior rate capability in sodium ions capacitor. It further demonstrates that the intercalation spacers in the interlayer of MXenes is an effective route for avoiding self-stacking, expanding interlayer spacing, and buffering volume expansion.

Results and Discussion

The Ti_2C intercalated by LAG molecules (LAG-Ti_2C) have been self-assembled by hydrogen-bond interaction between –OH/–F groups on the surface of Ti_2C and the $–NH_2$ groups in LAG molecules, as well as electrostatic interaction between negative charged surface of Ti_2C and the positive charged LAG (Figure 1a). The LAG molecules were intercalated into the interlayers of Ti_2C to not only prevent self-stacking between nanosheets and broaden interlayer spacing of Ti_2C, but also buffer structural expansion during charge/discharge process, guaranteeing the rapid insertion/extraction of Na^+ ions. To prove the successful introduction of LAG molecules into Ti_2C, Fourier transform infrared (FTIR) spectra was employed to analyze the groups of LAG-Ti_2C and Ti_2C (Figures 1b and S1). The new emergent absorption peaks at 3550 cm^{-1} of LAG-Ti_2C is attributed to stretching vibration of N–H bond, indicating that LAG molecules are successful introduced into Ti_2C to form LAG-Ti_2C substance. In addition, the introduced LAG molecules can also be proved via nitrogen element in X-ray photoelectron spectroscopy (XPS) spectra of LAG-Ti_2C compared with that of Ti_2C (Figure 1c). The C–N, $–NH_2$, and –NH– bonds are discovered in the high-resolution N 1s spectra of LAG-Ti_2C at 397.2, 399.0, and 400.0 eV, respectively, which are derived from intercalated LAG molecules (Figure 1d). The others bonding

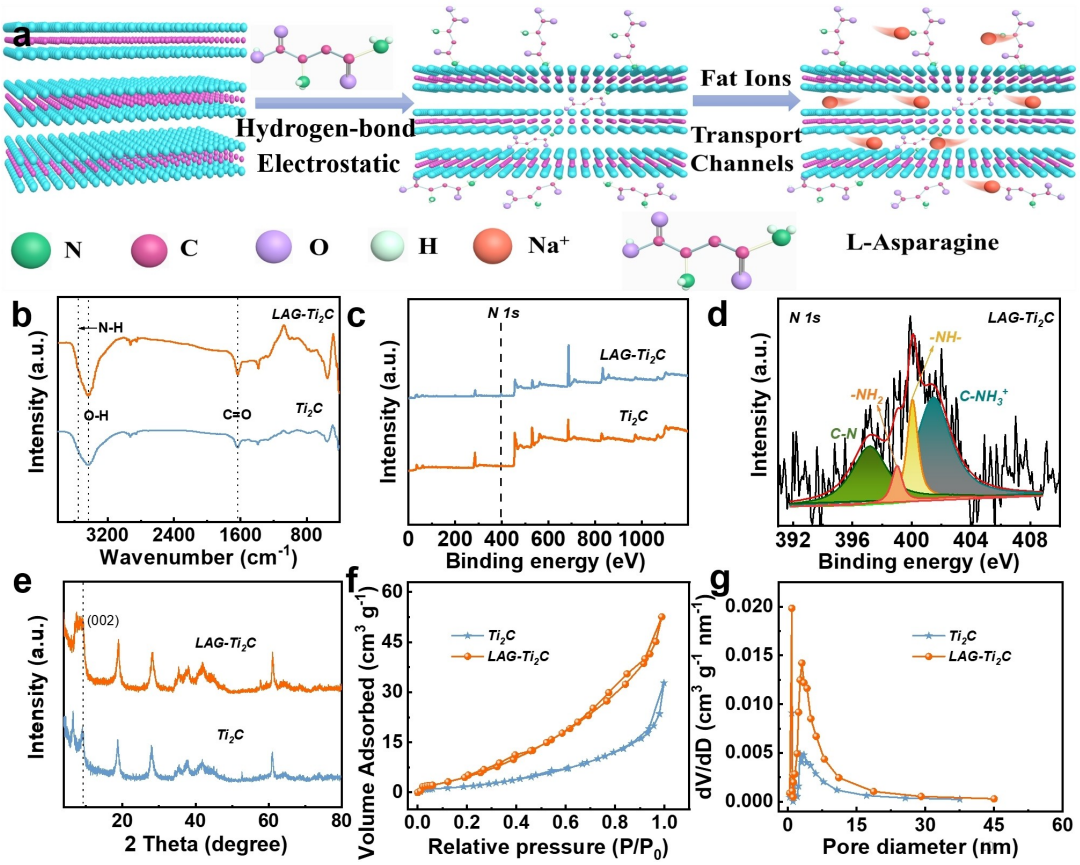

Figure 1. a) The schematic diagram of the synthesis of LAG-Ti_2C. b) FTIR spectra of LAG-Ti_2C and Ti_2C. c) The XPS spectra of LAG-Ti_2C and Ti_2C. d) The high-resolution XPS of N 1s for LAG-Ti_2C. e) The XRD patterns of LAG-Ti_2C and Ti_2C. f) The N_2 adsorption/desorption curves and g) the pore size distribution of LAG-Ti_2C and Ti_2C.

states of N in LAG-Ti_2C is mainly C-NH_3^+ at 401.5 eV, which refers to the protonated amine by hydrolyzing of LAG molecules. In addition, it can be found that LAG-Ti_2C and Ti_2C possesses the same peaks by comparing the high-resolution Ti 2p spectra, which suggests that there are no chemical bonds between Ti_2C and LAG molecules (Figure S2). The results of FTIR and XPS suggest that the LAG molecules intercalated LAG-Ti_2C substance via hydrogen-bond and electrostatic interaction have been successful prepared. According to the X-ray diffractometer (XRD) pattern, the (002) diffraction peaks of LAG-Ti_2C and Ti_2C appears at 8.3° and 9.04°, the calculated interlayer spacing is 1.06 nm and 0.98 nm, respectively (Figure 1e). The increased interlayer spacing of LAG-Ti_2C demonstrates that LAG molecules are successful intercalated into the interlayer of Ti_2C and deliver pillar effect to layered structure. The specific surface area of LAG-Ti_2C and Ti_2C are 19.6 and 9.6 $m^2 g^{-1}$, pore volumes are 0.081 and 0.051 $cm^3 g^{-1}$ by the measure of nitrogen adsorption/desorption, respectively (Figure 1f and g). Compared with Ti_2C, the increased specific surface area and pore volume of LAG-Ti_2C is also attributed to the introduction of LAG molecules that restrain self-stacking and enlarge interlayer spacing between Ti_2C sheets, which can increase the utilization of layered spaces.

A typical 2D layered structure of Ti_2C can be observed in the scanning electron microscopy (SEM) images (Figure 2a). However, the space between Ti_2C interlayers is unexposed owing to the self-stacking and aggregation between Ti_2C nanosheets (the "nanosheets" indicates a single Ti_2C layer in multilayer Ti_2C, which has been clearly labeled by red threads, Figure S3), which can result in low specific surface area and limited active sites for Na^+ ions storage. The 2D layered structure of Ti_2C is well inherited by LAG-Ti_2C, and LAG-Ti_2C exhibits looser layered structure than Ti_2C, as shown in Figure 2(b). The result indicates that LAG molecules have not destroyed the layered microstructure and only contribute pillar effect to Ti_2C. The pillar effect can expand interlayer spacing of Ti_2C and buffer structural expansion during Na^+ ions insertion process. Figure 2(c and d) are the low-resolution transmission electron microscopy (TEM) images, further manifesting the multilayer 2D layered structure of Ti_2C and LAG-Ti_2C. The measured interlayer spacing of LAG-Ti_2C and Ti_2C is 1.09 and 0.86 nm by HRTEM images, respectively, which is basically consistent with the XRD results (Figure 2e and f). The results further proved the pillar effect of LAG molecules between the interlayer of Ti_2C. In addition, the SEM mapping images exhibit the distribution of Ti,

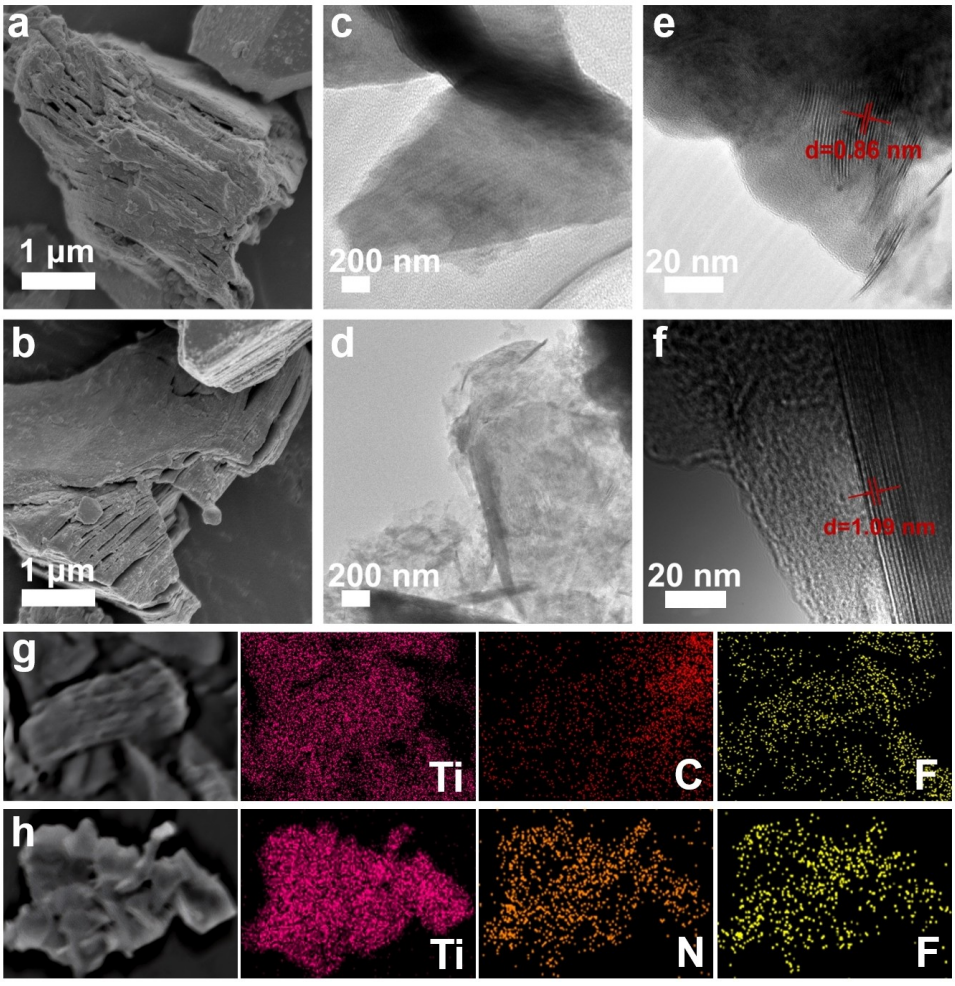

Figure 2. The SEM images of a) Ti_2C and b) LAG-Ti_2C. The TEM images of c) Ti_2C and d) LAG-Ti_2C. The HRTEM images of e) Ti_2C and f) LAG-Ti_2C. The SEM mapping images of g) Ti_2C and h) LAG-Ti_2C.

Research Article
doi.org/10.1002/batt.202300331
Chemistry Europe
European Chemical Societies Publishing

F, N, and O elements in LAG-Ti_2C and Ti_2C. Except the evenly dispersed Ti, C, and O elements, the N element originated from LAG molecules is also uniformly distributed, suggesting that LAG molecules have been uniformly interlayered in the Ti_2C interlayers (Figures 2g, h and S4).

Based on the excellent structure characteristics of LAG-Ti_2C, the electrochemical performance of LAG-Ti_2C and Ti_2C for Na^+ ions storage is compared in the voltage range of 0.01–3.0 V (vs. Na^+/Na, Figures 3a and S5a). In the initial cathodic scan at 0.1 mV s^{-1}, the reduction peak of LAG-Ti_2C and Ti_2C at 0.886 V is ascribed to the formation of irreversible and unstable solid electrolyte interphase (SEI) film, which is mainly responsible for a low initial Coulombic efficiency (ICE). Additionally, two pairs of obvious redox peaks at 1.0/1.2 V and 2.0/2.4 V can be discovered in CV curves of LAG-Ti_2C and Ti_2C, which are attributed to the insertion/extraction of Na^+ ions in the adjacent nanosheets and absorbed/dis-absorbed on the surface of nanosheets, respectively. Significantly, the CV curves of LAG-Ti_2C remain almost unchanged after the second cycle, suggesting excellent cycling stability and reversibility. Besides, the LAG-Ti_2C delivers a higher specific capacity of 113.5 mAh g^{-1} and capacity retention ratio of ~98.7% at a current density of 0.1 A g^{-1} after 1000 cycles (Figure 3b). By contrast, the specific capacity of Ti_2C is 82.3 mAh g^{-1}, and only maintains capacity retention ratio of 82.4%. The first galvanostatic charge-discharge (GCD) curves of LAG-Ti_2C and Ti_2C exhibits the irreversible discharge capacity of 199.1 and 177.8 mAh g^{-1} and ICE of 49.97% and 55.41%, respectively (Figures 3c and S5b). The reduced ICE of LAG-Ti_2C is attributed to more irreversible side reaction caused by the expanded interlayer spacing and the exposed more specific area. The third GCD curve of LAG-Ti_2C are completely overlapped with the second GCD curve, indicating the improved cycling stability and reversibility of LAG-Ti_2C, which is greatly agreed with CV curves. Figure 3(d and e) displays cycling performance of LAG-Ti_2C and Ti_2C at high current densities of 0.5, 1.0, 2.0, and 5.0 A g^{-1}, in which LAG-Ti_2C exhibits superior cycling stability (higher specific capacity and more stable CE) to Ti_2C. The improved specific capacity of LAG-Ti_2C is ascribed to the intercalation of LAG molecules that restrain self-stacking and widen interlayer spacing, which can expose more active sites for Na^+ storage and increase the utilization of layered structure. The increased capacity retention ratio and CE is due to the pillar effect of LAG molecules in Ti_2C interlayer, which can relieve the volume expansion and improve structural stability during Na^+ ions insertion/extraction processes. The reversible capacities of LAG-Ti_2C are 107.6, 91.8, 85.1, 78.6, 70.3 and 52.9 mAh g^{-1} at the different current densities of 0.1, 0.2, 0.5, 1.0, 2.0 and 5.0 A g^{-1}, while that of Ti_2C are 95.2, 84.4, 69.8, 56.3, 45.5, and 30.8 mAh g^{-1}, respectively (Figures 3f, g and S5c). Notably, LAG-Ti_2C still remains a high specific capacity of 113.0 mAh g^{-1} when the current density reduces

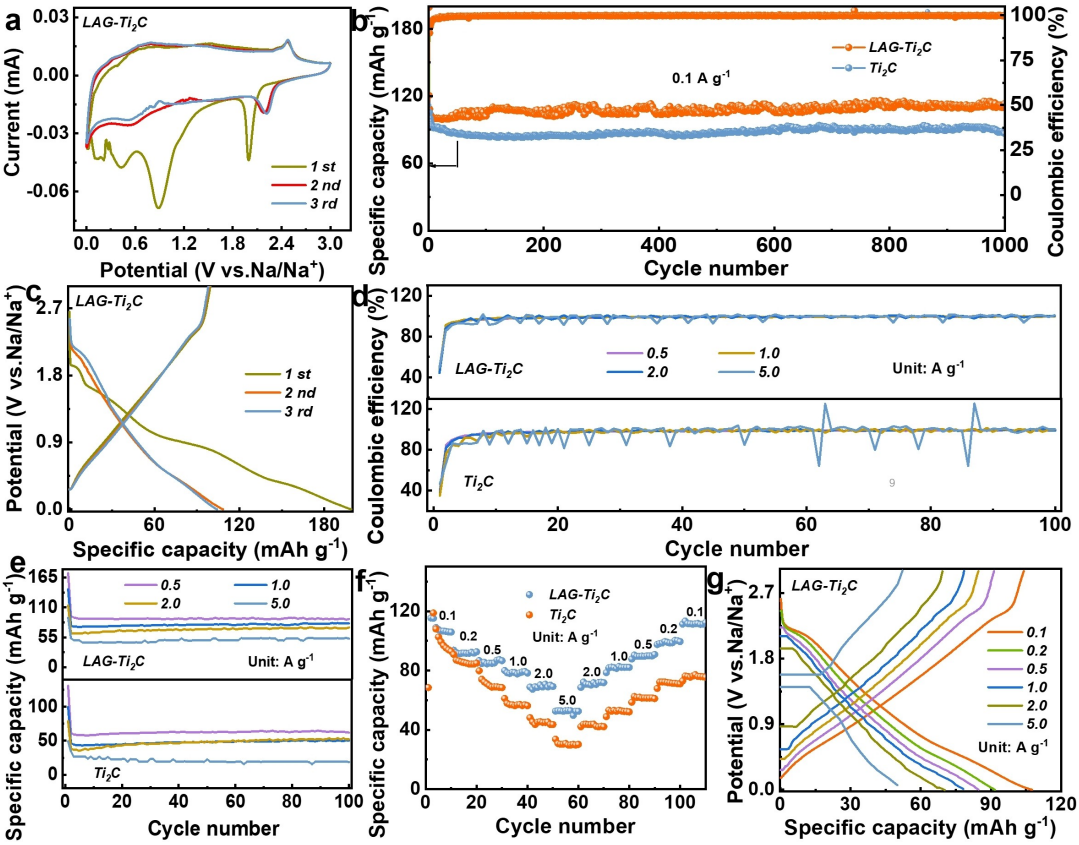

Figure 3. a) The first three CV curves of LAG-Ti_2C at scan rate of 0.1 mV s^{-1}. b) The long cycling stability of LAG-Ti_2C and Ti_2C at 0.1 A g^{-1}. c) The first three GCD curves of LAG-Ti_2C at current density of 0.1 A g^{-1}. d) CE and e) long cycling stability at the current densities of 0.5, 1.0, 2.0, and 5.0 A g^{-1}. f, g) The rate capability and corresponding to GCD curves of LAG-Ti_2C and Ti_2C.

Research Article
doi.org/10.1002/batt.202300331
Chemistry Europe
European Chemical Societies Publishing

from 5.0 A g^{-1} to 0.1 A g^{-1}, demonstrating high rate capability and reversibility of LAG-Ti_2C for Na^+ ions storage.

To explore the Na^+ ions storage mechanism in LAG-Ti_2C electrode, the CV curves at the different scan rates from 0.2 mV s^{-1} to 1.0 mV s^{-1} were measured (Figures 4a and S6a). The curves shape is remained with the increase of scan rate, demonstrating that LAG-Ti_2C possesses a rapid ion diffusion kinetics and low electrochemical polarization. To qualitatively explore the Na^+ ions storage mechanism, the relation between the peak current (i) and the corresponding scan rate (v) is explained by the following Equation (1):[24]

$$i = av^b \tag{1}$$

where a and b stand for variable parameters. The b value represents two storage behaviors: 1) $b = 1.0$, expressing that the Na^+ ions storage is dominated by surface-controlled capacity behavior; 2) $b = 0.5$, suggesting that the main Na^+ ions storage mechanism is typical diffusion-controlled capacity behavior. The calculated b values of LAG-Ti_2C and Ti_2C are 0.81/0.84 and 0.77/0.80 closed to 1.0 at the redox peaks, manifesting that the surface-controlled capacitive is predominant in LAG-Ti_2C and Ti_2C (Figures 4b and S6b). Furthermore, the surface-controlled capacity and diffusion-controlled capacity contribution can be further quantified by Equation (2) below:[34]

$$i(V) = k_1 v + k_2 v^{1/2} \tag{2}$$

where $k_1 v$ and $k_2 v^{1/2}$ means the surface-controlled capacity and diffusion-controlled capacity, respectively. The surface-controlled capacity contribution of LAG-Ti_2C increases from 77.3% at scan rate of 0.2 mV s^{-1} to 94.2% at scan rate of 1.0 mV s^{-1} (Figure 4c). In comparison, the surface-controlled capacity contribution of Ti_2C increases from 75.9% to 94.0% with the scan rate increased to 1.0 mV s^{-1} (Figure S6c). The LAG-Ti_2C delivers higher surface-controlled capacity contribution than Ti_2C due to the enlarged interlayer spacing, more exposed specific area, and abundant exposed active sites, which is also the reason why LAG-Ti_2C achieves high rate capability. The charge transfers resistance (R_{ct}) value of LAG-Ti_2C is adjacent with that of Ti_2C in Nyquist plots (Figure 4d), proving that the introduction of LAG molecules delivers a negligible impact on Na^+ ions storage reaction kinetics of Ti_2C. The Na^+ diffusion rate of LAG-Ti_2C and Ti_2C is qualitatively compared by the following Equations (3) and (4):[35,36]

$$Z_\omega = \sigma\omega^{-1/2} \tag{3}$$

$$D_{Na+} = \frac{R^2T^2}{2A^2n^4F^4C^2\sigma^2} \tag{4}$$

where σ, R, T, A, n, F, and C stand for Warburg coefficient, gas constant, absolute temperature, the surface area of electrode material, the number of electron transfer, Faraday constant, and the Na^+ ions concentration in electrolyte, respectively. According to Equation (3), the σ and Na^+ ions diffusion coefficient (D_{Na^+}) is negatively correlate. Thus, the value of σ gained by fitting Nyquist plots in low frequency region of LAG-Ti_2C (515.7) are lower than Ti_2C (824.9), revealing that the Na^+ ions diffusion rate of LAG-Ti_2C is more superior than Ti_2C (Figure 4e). To further confirmed the rapid Na^+ ions diffusion rate of LAG-Ti_2C, the Na^+ ions diffusion coefficient (D_{Na^+}) is quantitatively calculated from galvanostatic intermittent titration technique (GITT) curves by Equation (5).[37,38]

$$D = \frac{4L^2}{\pi\tau}\left(\frac{\Delta E_s}{\Delta E_t}\right)^2 \tag{5}$$

where L and τ are the thickness of active materials and relaxation time, ΔE_s stands for the potential difference between

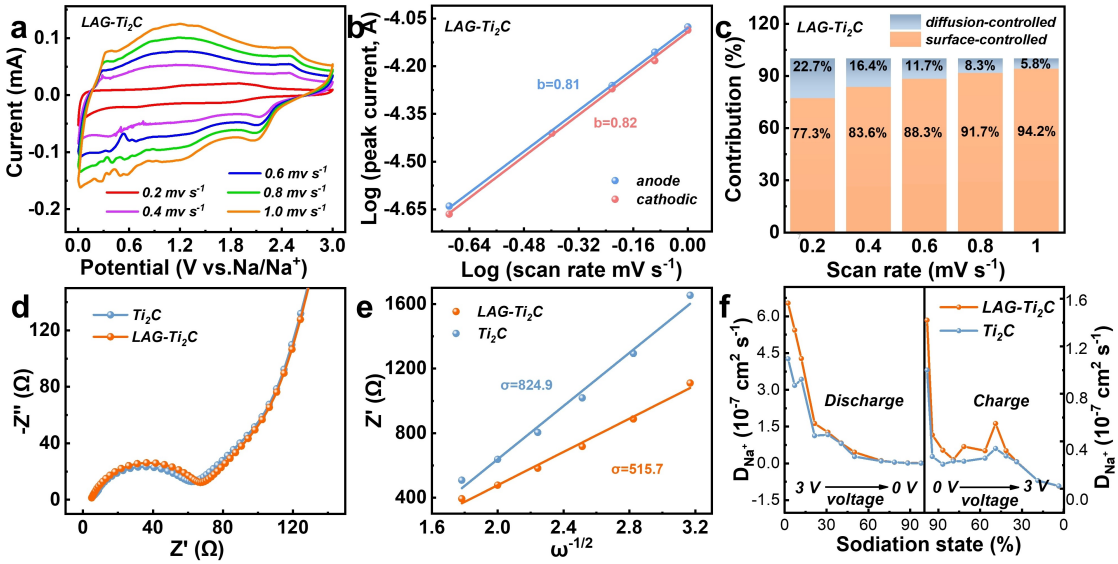

Figure 4. a) The CV curves of LAG-Ti_2C at the various scan rates. b) The b value of LAG-Ti_2C. c) The surface-controlled and diffusion-controlled capacity at the different scan rate. d) The Nyquist plots of Ti_2C and LAG-Ti_2C. e) The corresponding Nyquist plots of the real part of the -Z'' vs. $\omega^{-1/2}$ of Ti_2C and LAG-Ti_2C. f) The relationship between Na^+ ions diffusion coefficients and sodiation state in Ti_2C and LAG-Ti_2C.

Research Article
doi.org/10.1002/batt.202300331
Chemistry Europe
European Chemical Societies Publishing

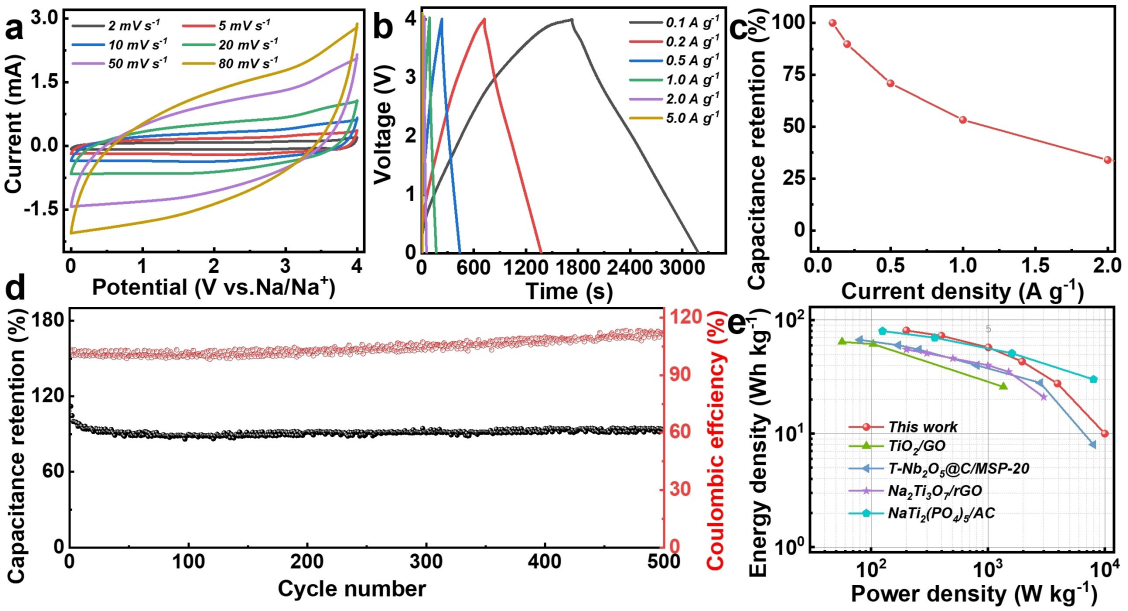

Figure 5. a) The CV curves of LAG-Ti_2C//AC SIC at various scan rates. b, c) The GCD curves and the specific capacity retentions at different current densities of LAG-Ti_2C//AC SIC. d) The cycling stability of LAG-Ti_2C//AC SIC at 1 A g^{-1}. e) The Ragone plots.

pulse time and relaxation time, and ΔE_t exhibits the potential change during relaxation time (Figure S7). In order to directly observe the Na^+ diffusion coefficient in charge and discharge state, the relationship between the Na^+ diffusion coefficient and sodiation state is displayed. At discharge process, the Na^+ diffusion coefficients in initial sodiation state (3 V) is larger than 100% sodiation state (0 V) since the expanded interlayer spacing of LAG-Ti_2C maintains spacious ions transport channels in interlayer and reduce diffusion barrier, which is favored to increase Na^+ diffusion coefficients. At charge process, the Na^+ diffusion coefficients in 100% sodiation state (0 V) is larger than initial sodiation state (3 V) since a large number of Na^+ in 100% sodiation state inevitably widen the layer spacing of Ti_2C to speed up the Na^+ diffusion. The LAG-Ti_2C exhibits larger D_{Na^+} (0.025–6.54×10^{-7} $cm^2 s^{-1}$) compared with Ti_2C (0.024–4.27×10^{-7} $cm^2 s^{-1}$) at various potential, confirming that the introduced LAG molecules can quicken Na^+ ions diffusion (Figure 4f). This is because that the widened interlayer spacing can broaden Na^+ ions diffusion channels in the interlayers of Ti_2C, and thus reducing Na^+ ions diffusion resistance.

In order to further clarify the outstanding electrochemical performance of LAG-Ti_2C, the LAG-Ti_2C//AC sodium ions capacitor (SIC) was assembled by using the LAG-Ti_2C anode, active carbon (AC) cathode, and 1.0 M $NaPF_6$ electrolyte. The discharge mechanism of LAG-Ti_2C//AC SIC at a large potential window of 0.01–4.0 V is that Na^+ ions are absorbed on the surface or inserted in the interlayer of LAG-Ti_2C anode, meanwhile the PF_6^- are absorbed on the surface of the AC cathode (Figure S8). The CV curves of LAG-Ti_2C//AC SIC at different scan rates of 2–80 mV s^{-1} are exhibited in Figure 5(a), in which the rectangular-like CV curves of LAG-Ti_2C//AC SIC indicates typical capacitor-type storage mechanism. The rectangular-like CV curves still are remained with the scan rates increase to 80 mV s^{-1}, indicating the high rate capability and reversibility. The symmetrical triangle-like GCD curves at different current densities can also reveal these capacitor-type storage mechanism (Figure 5b). The specific capacities of LAG-Ti_2C//AC SIC are 36.4, 32.7, 25.8, 19.4, and 12.4 F g^{-1} at the current densities of 0.1, 0.2, 0.5, 1.0, and 2.0 A g^{-1}, respectively. The specific capacity still remains 34.8% when the current density increased to 2.0 A g^{-1} (Figure 5c). Figure 5(d) displays the long cycling stability of LAG-Ti_2C//AC SIC, for which the capacitance retention of 93.4% and the CE of nearly 100.0% can be achieved at 1.0 A g^{-1} after 500 cycles, demonstrating the extraordinary cycling stability and reversibility of LAG-Ti_2C//AC SIC. Importantly, the LAG-Ti_2C//AC SIC delivers a high energy density of 27.56 Wh kg^{-1} at a super power density of 3937.1 W kg^{-1}, which are higher than that of previous reports such as TiO_2//GO,[39] T-Nb_2O_5@C//MSP-20,[40] $Na_2Ti_3O_7$//rGO,[41] $NaTi_2(PO_4)_5$//rGO (Figure 5e).[42]

Conclusions

In summary, the LAG molecules have been successfully intercalated into Ti_2C interlayers via hydrogen-bond and electrostatic interaction to construct LAG-Ti_2C. The intercalated LAG molecules contribute pillar effect to layered structure of Ti_2C, which can effectively restrain self-stacking, broaden interlayer spacing, and relieve structural expansion, realizing stable and rapid Na^+ ions storage. Consequently, the LAG-Ti_2C exhibits high specific capacity of 113.5 mAh g^{-1} and capacity retention ratio of ~98.7% after 1000 cycles at the current density of 0.1 A g^{-1}. The LAG-Ti_2C//AC SIC delivers a high energy density of 27.56 Wh kg^{-1} at a super high power density of 3937.1 W kg^{-1}. The work further proves that intercalation

spacers in interlayer of MXenes is an effective strategy to restrain self-stacking, widen interlayer spacing, and reduce structural expansion, which will optimize overall electrochemical performance for Na^+ ions storage.

Experimental Section

Materials preparation, materials characterization, and electrochemical measurements details are given in the supporting information.

Acknowledgements

This work was supported by the Applied Basic Research of Qinghai Province (2021-ZJ-737).

Conflict of Interests

The authors declare no conflict of interest.

Data Availability Statement

The data that support the findings of this study are available from the corresponding author upon reasonable request.

Keywords: Ti_2C · interlayer spacing · volume expansion · self-stacking · sodium ions capacitor

[1] X. Li, Z. Huang, C. E. Shuck, G. Liang, Y. Gogotsi, C. Zhi, *Nat. Chem. Rev.* **2022**, *6*, 389.
[2] M. Fang, J. Han, S. He, J.-C. Ren, S. Li, W. Liu, *J. Am. Chem. Soc.* **2023**, *145*, 12601.
[3] K. Yang, C. Li, H. Qi, Y. Dai, Y. Cui, Y. He, *J. Mater. Chem. A* **2023**, *11*, 10425.
[4] Y. Wang, T. Guo, E. Alhajji, Z. Tian, Z. Shi, Y.-Z. Zhang, H. N. Alshareef, *Adv. Energy Mater.* **2020**, *13*, 2202860.
[5] C. Li, S. Wang, X. R. Wang, W. Bai, H. Sun, F. Pan, Y. Chi, Z. Wang, *ACS Materials Lett.* **2023**, *5*, 2084.
[6] W. Y. Lieu, C. Lin, X. L. Li, S. Jiang, Y. Li, H. Y. Yang, Z. W. She, *Nano Lett.* **2023**, *23*, 5762.
[7] Z. Bayhan, J. K. El-Demellawi, J. Yin, Y. Khan, Y. Lei, E. Alhajji, Q. Wang, M. N. Hedhili, H. N. Alshareef, *Small* **2023**, 2208253.
[8] T. Xu, Y. Wang, K. Liu, Q. Zhao, Q. Liang, M. Zhang, C. Si, *Adv. Compos. Hybrid Ma.* **2023**, *6*, 108.
[9] M. Saraf, T. Zhang, T. Averianov, C. E. Shuck, R. W. Lord, E. Pomerantseva, Y. Gogotsi, *Small Methods* **2023**, 2201551.
[10] T. Wang, J. Zhao, L. Qi, G. Li, W. Yang, Y. Li, *Energy Storage Mater.* **2023**, *54*, 10.
[11] M. Li, X. Dai, M. Wang, H. Bai, *Small Methods* **2023**, 2300213.
[12] R. Guo, C. Chen, L. J. Bannenberg, H. Wang, H. Liu, M. Yu, Z. Sofer, Z. Lei, X. Wang, *Small Methods* **2023**, 2201683.
[13] J. Luo, C. Wang, H. Wang, X. Hu, E. Matios, X. Lu, W. Zhang, X. Tao, W. Li, *Adv. Funct. Mater.* **2019**, *29*, 1805946.
[14] P. A. Maughan, N. Tapia-Ruiz, N. Bimbo, *Electrochim. Acta* **2020**, *341*, 136061.
[15] M. R. Lukatskaya, O. Mashtalir, C. E. Ren, Y. D. Agnese, P. Rozier, P. L. Taberna, M. Naguib, P. Simon, M. W. Barsoum, Y. Gogotsi, *Science* **2013**, *341*, 1502.
[16] Y. Dong, H. Shi, Z. S. Wu, *Adv. Funct. Mater.* **2020**, *30*, 2000706.
[17] X. Wang, T. S. Mathis, K. Li, Z. Lin, L. Vlcek, T. Torita, N. C. Osti, C. Hatter, P. Urbankowski, A. Sarycheva, M. Tyagi, E. Mamontov, P. Simon, Y. Gogotsi, *Nat. Energy* **2019**, *4*, 241.
[18] T. Zhang, L. Chang, X. Xiao, *Small Methods* **2023**, 2201530.
[19] M. C. Liu, Y. S. Zhang, B. M. Zhang, L. B. Kong, Y. X. Hu, *J. Colloid Interface Sci.* **2022**, *612*, 267.
[20] M. Guo, C. Liu, Z. Zhang, J. Zhou, Y. Tang, S. Luo, *Adv. Funct. Mater.* **2018**, *28*, 1803196.
[21] X. Zhu, J. Shen, X. Chen, Y. Li, W. Peng, G. Zhang, F. Zhang, X. Fan, *Chem. Eng. J.* **2019**, *378*, 122212.
[22] Y. Zhao, C. Liu, R. Yi, Z. Li, Y. Chen, Y. Li, I. Mitrovic, S. Taylor, P. Chalker, L. Yang, C. Zhao, *Electrochim. Acta* **2020**, *345*, 136203.
[23] C. Wang, H. Jiu, L. Zhang, R. Xu, S. Che, Z. Guo, Y. Han, J. Ma, H. Li, F. Guo, *J. Alloys Compd.* **2023**, *8566*, 170332.
[24] M. C. Liu, Y. S. Zhang, B. M. Zhang, D. T. Zhang, C. Y. Tian, L. B. Kong, Y. X. Hu, *Renewable Energy* **2021**, *169*, 573.
[25] K. Ma, Y. Dong, H. Jiang, Y. Hu, P. Saha, C. Li, *Chem. Eng. J.* **2020**, *413*, 127479.
[26] Y.-Q. Wang, D.-T. Zhang, B. Zhao, H. Chen, C.-G. Chang, M.-C. Liu, *ACS Appl. Nano Mater.* **2023**, *6*, 3572.
[27] Q. Fu, X. Wang, N. Zhang, J. Wen, L. Li, H. Gao, X. Zhang, *J. Colloid Interface Sci.* **2018**, *511*, 128.
[28] H. Li, R. Chen, M. Ali, H. Lee, M. J. Ko, *Adv. Funct. Mater.* **2020**, *30*, 2002739.
[29] Y. Ding, Y. Chen, N. Xu, X. Lian, L. Li, Y. Hu, S. Peng, *Nano-Micro Lett.* **2020**, *12*, 54.
[30] Z. Ye, Y. Jiang, L. Li, F. Wu, R. Chen, *Chem. Eng. J.* **2022**, *430*, 132734.
[31] M. C. Liu, B. M. Zhang, Y. S. Zhang, B. N. Gu, C. Y. Tian, D. T. Zhang, Y. Q. Wang, B. Zhao, Y. Y. Wang, M. J. Liu, Y.-J. Yu, K. Zhao, L.-B. Kong, Y.-L. Chueh, *Mater. Today Energy* **2021**, *22*, 100832.
[32] M. C. Liu, D. T. Zhang, B. Liu, C. Y. Tian, B. Zhao, Y. Wang, Y. Wang, Y. Hu, L. B. Kong, D. Luo, Z. W. Chen, *Nano Energy* **2023**, *103*, 107795.
[33] M. C. Liu, B. M. Zhang, Y. S. Zhang, Y. X. Hu, *ACS Sustainable Chem. Eng.* **2021**, *9*, 12930.
[34] M. C. Liu, B. M. Zhang, Y. S. Zhang, D. T. Zhang, C. Y. Tian, L. B. Kong, Y. X. Hu, *Batteries & Supercaps* **2021**, *4*, 1473.
[35] Y. S. Zhang, B. M. Zhang, Y. X. Hu, J. Li, C. Lu, M.-J. Liu, K. Wang, L.-B. Kong, C.-Z. Zhao, W.-J. Niu, W.-W. Liu, K. Zhao, M.-C. Liu, Y. L. Chueh, *Energy Storage Mater.* **2020**, *34*, 45.
[36] B. Zhao, M.-C. Liu, D.-T. Zhang, Y.-Q. Wang, H. Chen, L.-B. Kong, C.-G. Chang, *Electrochim. Acta* **2022**, *440*, 141755.
[37] D.-T. Zhang, M.-C. Liu, J. Li, Y.-S. Zhang, B.-M. Zhang, C. Lu, Y.-X. Hu, K.-P. Wu, L.-B. Kong, *Electrochim. Acta* **2021**, *372*, 137860.
[38] N. Liu, X. Zhao, B. Qin, D. Zhao, H. Dong, M. Qiu, L. Wang, *J. Mater. Chem. A* **2022**, *10*, 25168.
[39] Z. Le, F. Liu, P. Nie, X. Li, X. Liu, Z. Bian, G. Chen, H. B. Wu, Y. Lu, *ACS Nano* **2017**, *11*, 2952.
[40] E. Lim, C. Jo, H. Kim, M. H. Kim, Y. Mun, J. Chun, Y. Ye, J. Hwang, K. S. Ha, K. C. Roh, K. Kang, S. Yoon, J. Lee, *ACS Nano* **2015**, *9*, 7497.
[41] S. Dong, L. Shen, H. Li, G. Pang, H. Dou, X. Zhang, *Adv. Funct. Mater.* **2016**, *26*, 3703.
[42] H. K. Roh, M. S. Kim, K. Y. Chung, U. Mani, V. Aravindan, S. Madhavi, K. C. l. Roh, K. B. Kim, *J. Mater. Chem. A* **2017**, *5*, 17506.

Manuscript received: July 25, 2023
Revised manuscript received: October 14, 2023
Accepted manuscript online: October 23, 2023
Version of record online: November 9, 2023